Numerical Simulation of Vapor Deposition Process of Perovskite Solar Cells: The Influence of Methylammonium Iodide Vapor Flow to Perovskite Growth

Rui Zhu
School of Marine Science and Technology,
Northwestern Polytechnical University,
Xi'an 710072, China
e-mail: ruizhu@mail.nwpu.edu.cn

Xiangyang Wei
State Key Laboratory of Precision Measurement
Technology and Instruments,
Department of Precision Instrument,
Tsinghua University,
Beijing 100084, China
e-mail: wei-xy14@mails.tsinghua.edu.cn

Gongnan Xie
School of Marine Science and Technology,
Northwestern Polytechnical University,
Xi'an 710072, China
e-mail: xgn@nwpu.edu.cn

Terrence Simon
Department of Mechanical Engineering,
University of Minnesota,
Minneapolis, MN 55455
e-mail: simon002@umn.edu

Tianhong Cui[1]
Department of Mechanical Engineering,
University of Minnesota,
Minneapolis, MN 55455
e-mails: cuixx006@me.umn.edu;
cuixx006@umn.edu

This paper presents a two-dimensional (2D) transient numerical model for simulating the vapor deposition process for growing perovskite films. The diffusion process of methylammonium iodide (MAI) vapor through the processing chamber to react with the lead iodide (PbI_2) substrate and grow the perovskite layer is analyzed with a diffusion coefficient that has been determined by measuring thicknesses of perovskite layers grown in a chemical vapor deposition (CVD) chamber. Innovations applied to the CVD chamber to improve the uniformity of layer thickness and offer control over the growth process are applied and computationally assessed. One is the addition of screens at various strategic locations in the chamber to improve flow uniformity. Another is changing the locations of MAI sublimation bowls and chamber outlet numbers and locations. The results show that adding screens makes the MAI vapor flow more uniform in the plenum while allowing a quicker purge of the N_2 inert gas. This leads to a higher and more uniform growth rate of perovskite. The MAI vapor flow is influenced by the reaction plenum geometry, so the chamber is expected to allow good control of the process to achieve uniform surface deposition rate and controlled grain growth of the perovskite layer. [DOI: 10.1115/1.4047296]

Keywords: perovskite solar cells, chemical vapor deposition, perovskite layer growth, surface deposition rate, transient numerical simulation, efficiency, solar

1 Introduction

Perovskite solar cells have drawn tremendous attention because of their excellent properties such as tunable bandgap, long carrier diffusion length, excellent light absorption performance, low cost, low-temperature processing, and flexible materials. The power conversion efficiency (PCE) of perovskite solar cells has rapidly improved from 3.8% to 25.2% in recent years [1,2], which is close to the best single crystalline silicon solar cells. The next step for researchers is to develop a low-cost and large-scale processing procedure for large-area, high-performance, and stable perovskite solar cell fabrication to make this technology more competitive in commercial applications than for other solar cells, like silicon-based solar cells, CdTe-based solar cells, and so on.

There are many factors that have significant impacts on perovskite solar cell performance, including the perovskite film morphology, crystallinity, thickness, and material purity. To produce high-quality, uniform perovskite films with fewer defects, different kinds of methodologies have been developed, such as the one-step solution method [3–5], the two-step solution method [6,7], the vapor-assisted solution process [8,9], dual-source vacuum deposition [10,11], and hybrid deposition [12]. Among these methodologies, the solution processes are the most popular, and high efficiencies are achieved. However, the solution processes have high uncertainties in the process, making commercial applications challenging. The vapor-assisted deposition technique has more effective control over the working conditions, like pressure,

temperature, and heat and mass transfer, which is beneficial for achieving stable and high-performance perovskite solar cells. Besides, as precursor organic and inorganic materials have different boiling points, the vapor-assisted deposition method is more controllable than the dual-source vapor deposition method. Overall, the vapor-assisted hybrid physical–chemical deposition method is more favorable for its higher stability and controllability and higher possibility for commercial application.

Yang and coworkers introduced the methylammonium iodide (MAI) vapor-based approach and named it as vapor-assisted solution processing for the fabrication of the perovskite layer [13–15]. In the process, PbI_2 substrates were reacted with MAI vapor at 150 °C in an N_2 environment for 2 h. The perovskite layers they produced show high crystallinity, large grain size, and uniform surface coverage. The high-quality $CH_3NH_3PbI_3$ perovskite films enhanced the performance of the solar cells from their device with a PCE of 12.1%. Wang et al. [16] systematically studied how the chemical vapor deposition (CVD) process affects the perovskite film property. They changed the substrate temperature, the postannealing condition, and the evaporation source materials. In their experiments, the CH_3NH_3I quartz crystal microbalance (QCM) was placed facing downward and directly above the CH_3NH_3I vapor source. There was a shutter between the CH_3NH_3I QCM and the MAI source to better control the MAI evaporation rate during a long deposition period (1 h). Their results showed that the vapor-assisted deposition process needed careful control and when optimized led to the fabrication of the high-quality perovskite film. The evaporation rate of MAI (CH_3NH_3I) is an important factor in this process, but needs better control during the formation of perovskite.

Lower working pressure leads to a higher sublimation rate of organic halide and a larger diffusion rate, which increases the deposition rate and the uniformity of the perovskite growth. Leyden et al. [17] used a two-step CVD method to grow perovskite

---

films with low working pressure. A two-zone furnace was used in their study. The MAI precursor was placed in one zone with a temperature of 185 °C, while the substrates are placed in the other zone with a lower temperature of 145–170 °C. The working pressure was 100 Pa, and nitrogen was used as the carrier gas. The two-zone furnace increased the deposition rate because the vapor pressure of the organic halide could be controlled independently. The reported nominal reaction time was 1 h. The same group used formamidinium iodide to fabricate perovskite solar cells with a heating time of the organic components of less than 30 min [18]. The best PCE reported is 14.2%. Low pressures also reduce the required reaction temperature, since the sublimation temperature of an organic halide is reduced at lower pressures. Peng et al. [19] used the hybrid vapor-assisted method and fabricated high-performing cells with a PCE of 14.7%. Both their working pressure and temperature are low: 0.3 Pa and 82 °C, respectively. Their study showed that low pressure can reduce the reaction temperature since the sublimation rate of MAI decreases with lower pressure. However, low working pressure and temperature increase the required reaction time.

The performance of a perovskite solar cell is highly influenced by the crystalline quality of the perovskite thin film sandwiched between electron and hole transport layers in a typical perovskite solar cell structure. The crystalline quality is characterized by the crystal grain size and the uniformity of film thickness [20,21]. Although many studies have been done recently on lead halide perovskite nanocrystals, there are still significant gaps in understanding of nucleation and growth processes involved in the formation of perovskite, as well as the relationship between the perovskite crystal structure and the solar cell performance. Agrafiotis et al. [22] tested the thermochemistry properties including the reaction enthalpy of Ca-Mn-based perovskites. Udayabhaskararao et al. [23] used $CsPbX_3$ as a model system to study the formation mechanism of cubic $CsPbX_3$ nanocrystals, their growth via oriented attachment into larger nanostructures, and their associated phase transformations. It was found that the formation of $CsPbX_3$ nanocubes occurs through the seed-mediated nucleation method, where Pb nanoparticles formed during the reaction act as seeds. Further growth occurs through self-assembly and oriented attachment.

The processing temperature and pressure are critical to the formation of uniform and stable perovskite films. Xue et al. [24] conducted a Monte Carlo simulation to study the influence of device geometry, material properties, and operating conditions on the performance of a perovskite solar cell. It was found that the hole mobility in the hole transport layer and the layer thicknesses of the hole and electron transfer layers are the three most important parameters influencing the performance of perovskite solar cell. Yang et al. [25] numerically studied the influence of operating pressure and temperature on the surface deposition rate of perovskite films. The results show that the increasing operating temperature and pressure will increase the surface deposition rate of perovskite. An optimized mass flow configuration was proposed by adding a flow resistance to give a more uniform distribution of MAI vapor flow inside the reaction chamber. Arivazhagan et al. [26] studied the influence of pressure in the CVD process and found that the operating pressure has strong effects on the grain size of the grown perovskite film. They also proposed a method to enhance the perovskite grain size by a gradual change in vapor pressure.

Perovskite solar cells have been rapidly developing in recent years. Currently, the vapor-assisted deposition process is the best way to achieve large and high-quality perovskite films. The process has the advantage of lower temperature processing than used with spin coating. This gives more flexibility in choices for materials for the remainder of the cell, including flexible materials. This article continues to study the vapor deposition process of the perovskite layer by numerical simulation. In this work, hybrid physical–chemical vapor deposition of planar methylammonium lead iodide ($MAPbI_3$) is grown using a MAI precursor vapor. The diffusion process of MAI vapor through the growing perovskite layer is analyzed with a diffusion coefficient calculated by measuring the

thickness of the perovskite layer with different growing times. The influences of adding screens at different locations in the plenum and changing the inlet and outlet numbers and locations on the uniformity of the perovskite layer growth rate are analyzed by using computational fluid dynamics and mass transfer. This study helps understand the physics of the vapor deposition process of the perovskite film growth and provide a method to predict and control the surface deposition rate by controlling the working conditions.

2 Numerical Model

2.1 Physical Model and Boundary Conditions. In the reactor, a quartz box is put inside a chamber heated by surrounding heating elements to realize temperature control during the sublimation process. The chamber is first evacuated to a desired pressure, and then nitrogen (N_2) is introduced into the chamber to purge the particles and atmospheric gases. Then the nitrogen flow is shut down, and the heating element is turned on to heat the quartz box to a specific temperature, while a low near-vacuum pressure is maintained in the box. During the heating process, MAI powder in the crucibles sublimates into the quartz box and then mixes and diffuses within the N_2 atmosphere. The mixture of MAI and N_2 flows around the substrate surfaces, which are coated with PbI_2, and then to an outlet. A deposition reaction takes place on the substrate surface, and a layer of perovskite is formed. As the MAI powder continues to sublimate, the quartz box becomes filled with MAI vapor, while the N_2 from its initial charge is purged, finally reaching a steady-state with a steady outflow of pure MAI and a continuous MAI concentration for deposition into the perovskite film on each substrate surface.

To simulate this process, a simplified 2D transient model is established, as shown in Fig. 1. The reaction plenum is a rectangular box with a length of 156 mm and a height of 60 mm. It has three inlets and three outlets. Each inlet is 20 mm wide and 10 mm high, and each outlet is 5 mm wide and 5 mm high. Two screens are put in the plenum, as the figure shows, to make the flow from upper plenum to lower plenum more uniform. The two substrates are 10 mm above the second screen, and each substrate is 20 mm wide and 2 mm thick. The box is initially filled with N_2. From the beginning of the simulation, pure MAI vapor is introduced through the inlets, simulating the sublimation process of the actual system. The N_2 is purged, and finally, the box is filled with MAI vapor. The two substrates are initially coated with PbI_2. The reaction is on the surfaces of the PbI_2 substrates when MAI vapor becomes available.

The computational mesh used in this study is made by ANSYS ICEM 18.2. The mesh has 26,111 nodes, verified to be enough by a mesh-independence test. The commercial computational fluid dynamics software ANSYS FLUENT 18.2 is used for this numerical simulation. The operating pressure and the temperature are set as
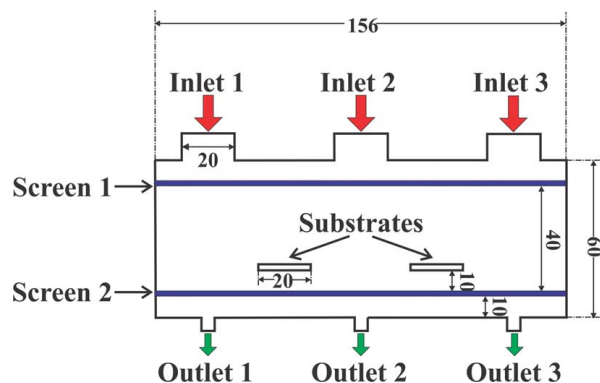

Fig. 1 The geometry of the numerical model used in the simulation

Table 1 Material property of MAI, PbI$_2$, and perovskite MAPbI$_3$ [25]

	MAI	PbI$_2$	MAPbI$_3$
Density (kg/m^3)	Idea gas	6160	4000
Specific heat (J/kg K)	498	173	304.85
Thermal conductivity (W/m K)	0.00672	0.73	0.5
Viscosity (kg/m s)	1.243×10^{-5}	1×10^{20}	1×10^{20}
Molecular weight (g/mol)	159	461	620
Standard state enthalpy (J/kmol)	-3.3×10^{-8}	-2.03×10^{-8}	-5.07×10^{-8}
Standard state entropy (J/kmol K)	250,000	174,850	200,000
L-J characteristic length (angstrom)	5.2	5.5	6
L-J energy parameter (K)	478.3	400	550

0.4 Torr (53.33 Pa) and 378.15 K (105 °C), respectively. The properties of MAI vapor are estimated using the Joback estimating approach [27]. The properties of PbI$_2$ and MAPbI$_3$ are adapted from the literature [28,29]. Table 1 lists the material property used in this study. The inlet condition is set as a pressure inlet with a constant total pressure of 0.1 Pa. The outlets are set with pressure outlet conditions. All the walls are of a constant and uniform temperature. The screens are set as porous-jump boundaries. The porous-jump boundary is a one-dimensional simplification of the porous media model used to model pressure drops through screens. The pressure change is defined as a combination of Darcy's law and an additional inertial loss term:

$$S_i = \sum_{j=1}^{3} D_{ij} \mu v_j + \sum_{j=1}^{3} C_{ij} \frac{1}{2} \rho |v_j| v_j \qquad (1)$$

where μ is the viscosity, v is the velocity of the approach flow to the screen, ρ is the density, and D and C are prescribed matrices for Darcy and inertial coefficients, respectively, of the modified Darcy equation.

For a uniform porous medium, Eq. (1) can be simplified as follows:

$$S_i = \frac{\mu}{k} v_i + C_2 \frac{1}{2} \rho |v_j| v_j \qquad (2)$$

where k is the permeability and C_2 is the inertial resistance factor. In a laminar flow with very low Reynolds number, the inertial loss term is negligible. The permeability is calculated by an empirical formula based on the screen type, opening ratio, and thickness [30], which is 3×10^{-7} m^2 in this study.

Six cases are analyzed to characterize the flow field, diffusion, and mixing processes of MAI vapor during the deposition process. The MAI diffusion through the perovskite layer to the reaction layer and the perovskite growth rate are also analyzed. Furthermore, the analysis helps assess the effectiveness of screens toward making the surface deposition rate of MAPbI$_3$ (perovskite) uniform over the substrates. For cases 1–4, all three inlets and only the middle outlet are open. Case 1 has no screen. Case 2 has the upper screen (screen 1), while case 3 has the lower screen (screen 2). Case 4 has two screens (screens 1 and 2). Both cases 5 and 6 have two screens (screens 1 and 2). For case 5, inlets 1 and 3 and outlet 2 are open, while for case 6, inlet 2 and outlets 1 and 3 are open. These cases are summarized in Table 2.

Table 2 Different case settings

Case	Inlet	Outlet	Screen
1	1, 2, 3	2	No screen
2	1, 2, 3	2	1
3	1, 2, 3	2	2
4	1, 2, 3	2	1, 2
5	1, 3	2	1, 2
6	2	1, 3	1, 2

2.2 Reaction Model. A laminar flow model is used in this simulation. A species transfer model is used to calculate the mass transfer of MAI and N$_2$.

The governing equations for fluid flow and energy can be expressed as follows:

Continuity equation:

$$\frac{\partial}{\partial t}(\rho Y_i) + \nabla \cdot (\rho \vec{v} Y_i) = -\nabla \cdot \vec{J}_i + R_i \qquad (3)$$

where Y_i is the local mass fraction of each species, R_i is the net rate of production of species i by chemical reaction, and J_i is the diffusion flux of species i, which arises due to gradients of concentration and temperature, as follows:

$$\vec{J}_i = -\rho D_{i,m} \nabla Y_i + D_{T,i} \frac{\nabla T}{T} \qquad (4)$$

where $D_{i,m}$ is the mass diffusion coefficient for species i in the mixture and $D_{T,i}$ is the thermal diffusion coefficient.
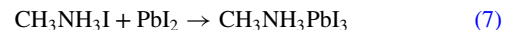
Momentum equations:

$$\frac{\partial(\rho u)}{\partial t} = -\nabla p + \rho F + \mu \Delta u \qquad (5)$$

Energy equation for fluid:

$$\frac{\partial}{\partial t}(\rho E) + \frac{\partial}{\partial x_i}[u_i(\rho E + p)] = \frac{\partial}{\partial x_i}\left(k\frac{\partial T}{\partial x_i} - \sum_i h_i J_i - u_j(\tau_{ij})_{eff}\right) \qquad (6)$$

where J_i is the diffusion flux of species i.

A wall surface reaction model is used to calculate the surface deposition process of perovskite. The reaction equation is as follows:

$$CH_3NH_3I + PbI_2 \rightarrow CH_3NH_3PbI_3 \qquad (7)$$

Under the operating conditions of the present cell, there is no backward reaction, only forward reaction. The reaction rate constant is defined by the Arrhenius equation:

$$k_{arr} = A_{pre} e^{-E_a/RT} \qquad (8)$$

where A_{pre} is the pre-exponential factor, E_a is the activation energy, and R is the gas constant. The activation energy E_a was found to be 110 kJ/mol in Ref. [31]. The pre-exponential constant, A, at our operating conditions is found by measurements, as will be discussed.

In the reaction process, a solid layer of MAPbI$_3$ will grow on the substrates. The MAI vapor must diffuse through the solid layer to react with the PbI$_2$. To simulate the diffusion process, the diffusion coefficient of MAI vapor through perovskite layer must be found. The diffusion process is schematically shown in Fig. 2. The first step is from face 1 to face 2. The MAI vapor is transferred from the bulk of the gas phase to the gas–solid interface. The mass flux, J_1, in this step is defined as follows:

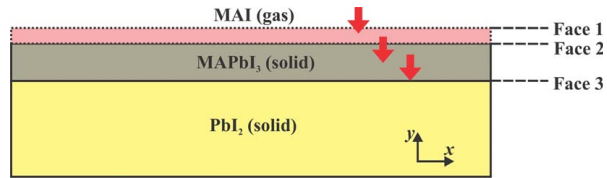$$J_1 = h_1 \frac{\partial C_{MAI}}{\partial y} \qquad (9)$$

Fig. 2 Diffusion process in the deposition reaction of perovskite

where h_1 is the mass transfer coefficient of MAI vapor and C_{MAI} is the concentration of MAI. The second step is from face 1 to face 2. The MAI vapor diffuses through the perovskite layer to the PbI$_2$ layer. The mass flux, J_2, in this step is defined as follows:

$$J_2 = D \frac{\partial C_{MAI}}{\partial y} \tag{10}$$

where D is the diffusion coefficient of MAI vapor through the perovskite layer. The third step is on face 3. The MAI reacts with PbI$_2$ and grows the perovskite layer. The consumption rate of MAI, J_3, in this step is represented as follows:

$$J_3 = kC_{MAI} \tag{11}$$

where k is defined as a reaction constant multiplied by the concentration of PbI$_2$, $k_{arr}C_{PbI_2}$. The surface concentration of PbI$_2$ coated on the substrates is C_{PbI_2}. It is estimated from the density and the crystal structure of PbI$_2$.

As an approximation, we may assume that at steady-state, the bulk concentration of MAI is uniform, and the mass of MAI transferred through the MAPbI$_3$ layer is equal to the mass of MAI consumed by the deposition reaction. By combining Eqs. (9)–(11), we can obtain the following equation:

$$d^2 + \left(\frac{D}{h} + \frac{D}{k}\right)d = \frac{DC_1}{N}t \tag{12}$$

where d is the thickness of the MAPbI$_3$ layer, C_1 is the concentration of MAI at face 1, and t is the reaction time. In this expression, N is the number of MAI molecules incorporated into a unit volume of the MAPbI$_3$ layer, equal to $\rho(\text{MAPbI}_3)/M(\text{MAPbI}_3)$. If we define as new constants, $A = D/h + D/k$, and $B = DC_1/N$, Eq. (12) can be simplified as follows:

$$d = B\frac{t}{d} - A \tag{13}$$

Therefore, if we measure the thickness of the perovskite layer at several times after the steady-state growth has begun, we can evaluate the values of A and B by fitting the thickness versus time data with Eq. (13) and calculating the diffusion coefficient D.

After finding the value of the diffusion coefficient D, we use it in our numerical simulation. In our simulation, we use a stepwise method to include the effects of the growing thickness of perovskite, as Table 3 presents, realized by the user-defined function. The concentration of MAI at face 2 is C and C^* is the concentration of MAI at face 3, which is calculated by Eqs. (10) and (11). The thickness of the perovskite layer is represented as d. The surface

Table 3 Iteration process to calculate the surface deposition rate of perovskite

t	C	C^*	d	SDR	J
t_0	C_{t0}	$C^*_{t0} = C_0$	$d_{t0} = 0$	SDR$_{t0}$ (Eq. (3))	J_{t0}
t_1	C_{t1}	$C^*_{t1} = DC_1/$ $(kd_1 + D)$	$d_{t1} = d_{t0} +$ SDR$_{t0}\Delta t$	SDR$_{t1}$	J_{t1}
			......		

deposition rate of MAPbI$_3$ (SDR) is calculated as follows:

$$\text{SDR} = \frac{kC^*M(\text{MAPbI}_3)}{\rho(\text{MAPbI}_3)} \tag{14}$$

where M is the molecular weight of MAPbI$_3$. J in Table 3 is the mass flux or mass consumption of MAI. At the beginning of the simulation, $t = t_0$, the thickness of the perovskite layer is 0, and $C = C^*$, and then, J_{t0} and SDR$_{t0}$ can be calculated. After a short time-step, Δt, when $t = t_1$, the thickness of the perovskite layer, d_{t1}, and C^*_{t1} can be calculated based on SDR$_{t0}$ and C_{t1}. Then, the new SDR and J can be calculated. This process proceeds for the successive time-steps.

2.3 Fabrication and Thickness Measurement of Perovskite. For evaluation of the diffusion coefficient, D, the thickness of the perovskite films versus time must be measured. The films to be measured are fabricated on a substrate with TiO$_2$/fluorine-doped tin oxide (FTO)/glass. First, FTO transparent conductive glass substrates (Nippon sheet glass, 14 Ω) are cleaned with the deionized water, ethanol, acetone, and isopropyl alcohol sequentially for 30 min in an ultrasonic bath. Then, about 15 min of oxygen plasma processing is used to chemically remove the organic compounds and other residues from the surfaces of the substrates by the Technics Oxygen Asher. Following this, a TiO$_2$ film is fabricated on the FTO/glass as soon as possible after the oxygen plasma treatment is completed. The TiO$_2$ film is deposited twice by spin coating a solution prepared by dissolving 502.5 μL titanium diisopropoxide bis (acetylacetonate) (75 wt% in isopropanol) into 6.35 mL 1-butanol. Each spin coating process is done with a speed of 2000 rpm for 30 s. After each spin coating process, the substrates are baked with a temperature of 140 °C for 10 min before the next step. Then, the substrates are sintered in a CVD tube with a temperature of 550 °C for 60 min. After sintering, the TiO$_2$ film is cleaned by the oxygen plasma treatment for 5 min. Finally, the perovskite films are deposited on the TiO$_2$ film substrates. They are fabricated by a hybrid physical–chemical deposition process. First, the PbI$_2$ film is deposited on the TiO$_2$/FTO/glass by a spin coating method. A 1.3 M PbI$_2$/DMF (N, N-dimethylformamide) solution is spin coated with a speed of 4000 rpm for 30 s. Then, the substrates are baked for 15 min with a temperature of 70 °C. The perovskite film growth process proceeds in a tube furnace (OTF-1200X, MTI Corporation). The substrates, with PbI$_2$ films, are put into a quartz tube evenly filled with CH$_3$NH$_3$I powder (Greatcell Solar Limited), and then, the tube furnace is sealed. When the reaction time has reached the set value, the mechanical pump is opened to end the reaction. During the fabrication process, five samples of PbI$_2$ perovskite films are prepared. They are as follows: pure PbI$_2$ (group 0) film, PbI$_2$ and perovskite films with reaction times of 180 min (group 1), 240 min (group 2), 300 min (group 3), and a pure perovskite film with a reaction time more than 600 min (group 4). In the previous results [32], the PbI$_2$ film was completely transformed to CH$_3$NH$_3$PbI$_3$ film when the reaction time was more than 420 min.

The above processing gives the thickness versus the time data for the perovskite film growth in the environment of the vapor deposition chamber. The process for determining thicknesses is shown in Fig. 3. The thickness of pure PbI$_2$ film (group 0) is d_0. After all the PbI$_2$ is transformed to MAPbI$_3$, the thickness of the pure perovskite layer (group 4) is d_4. The thicknesses of the combination of PbI$_2$ and perovskite film with different reaction times t ($t = 180$, 240, and 300 min) are d_t. When the reaction time is t, the thickness of the growth perovskite layer is d_{t,MAPbI_3} and the thickness of the unreacted PbI$_2$ is d_{t,PbI_2}. Then, we have the following equation:

$$d_t = d_{t,\text{MAPbI}_3} + d_{t,\text{PbI}_2} \tag{15}$$

We assume that the ratio of the thickness of the growth of the perovskite layer and the thickness of PbI$_2$ reacted, d_4/d_0, is constant.

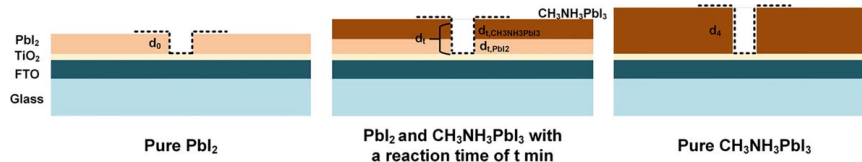**Fig. 3 Schematic diagram of the measurement procedures for determining the thickness of growth of the perovskite layer**

Table 4 Thickness of PbI$_2$ and perovskite films for the five groups

Group	Types of films	Reaction time (min)	Thickness (nm)
0	Pure PbI$_2$	0	212.70
1	PbI$_2$ and perovskite film	180	382.68
2	PbI$_2$ and perovskite film	240	429.21
3	PbI$_2$ and perovskite film	300	471.70
4	perovskite film	>600	531.09

Table 5 Thickness of growth perovskite layer at different reaction times

Group	Types of films	Reaction time (min)	Thickness of growth perovskite film (nm)
1	PbI$_2$ and perovskite film	180	283.53
2	PbI$_2$ and perovskite film	240	361.15
3	PbI$_2$ and perovskite film	300	432.02

So, at the time t, the thickness of the perovskite layer is equal to the thickness of the reacted PbI$_2$ multiplied by this ratio. Then, we can have the following equation:

$$d_{t,\text{MAPbI}_3} = (d_0 - d_{t,\text{PbI}_2}) \frac{d_4}{d_0} \qquad (16)$$

The thicknesses d_0, d_t, and d_4 are measured, and the thickness of the perovskite layer, d_{t,MAPbI_3}, is calculated as follows:

$$d_{t,\text{MAPbI}_3} = d_4 \frac{d_4 - d_0}{d_t - d_0} \qquad (17)$$

Sharp tweezers are used to remove steps in the five films, and then a surface profile measurement system is used to measure the thicknesses of each of the five films. The measured thicknesses are presented in Table 4. Finally, the thicknesses of the grown perovskite layers are calculated by Eq. (17), and the results are presented in Table 5.

By using Eqs. (12) and (13) and the results presented in Table 5, the constants A and B are found to be 1298 and 41.551, respectively. One thing that should be noticed here is that the value of the two constants will be different if one uses different dimensions or the operating conditions are different. The diffusion coefficient of MAI vapor through the perovskite layer under the operating conditions can be computed through Eq. (13) as 1.58×10^{-11} m^2/s, which is a reasonable value for gas diffusing in solid. The pre-exponential factor A_{pre} is 1.93×10^{16}, which is near the value used by Wang et al. [31], that is, 9×10^{15}. Figure 4(a) shows the thickness of the perovskite layer over time as calculated by Eq. (13) using the above values for diffusivity and pre-exponential factor from the experimental measurements. We can see that the experimental points lie on the theoretical model curve perfectly. Figure 4(b) shows the growth of thickness of the perovskite layer over time calculated by Eq. (13) and by numerical simulation. They agree well. We also tried to directly fit the experimental points with our numerical simulation. The value of the diffusion coefficient backed out from that analysis is 1.3×10^{-11}. It is suitably close to the value computed from the analytical model presented earlier. The difference may come from the following: (1) the pressure and concentration calculated by the numerical simulation may be slightly different from that we used in the theoretical model; (2) the mass transfer coefficient in the gas phase calculated by numerical simulation may be different from that we used in the theoretical model; and (3) there may be errors caused by the calculation method in the numerical simulation.

3 Results and Discussion

Figure 5 shows the average surface deposition rate and thickness of MAPbI$_3$ layer on the substrates over time for all the cases. For each case, the surface deposition rate first increases and then
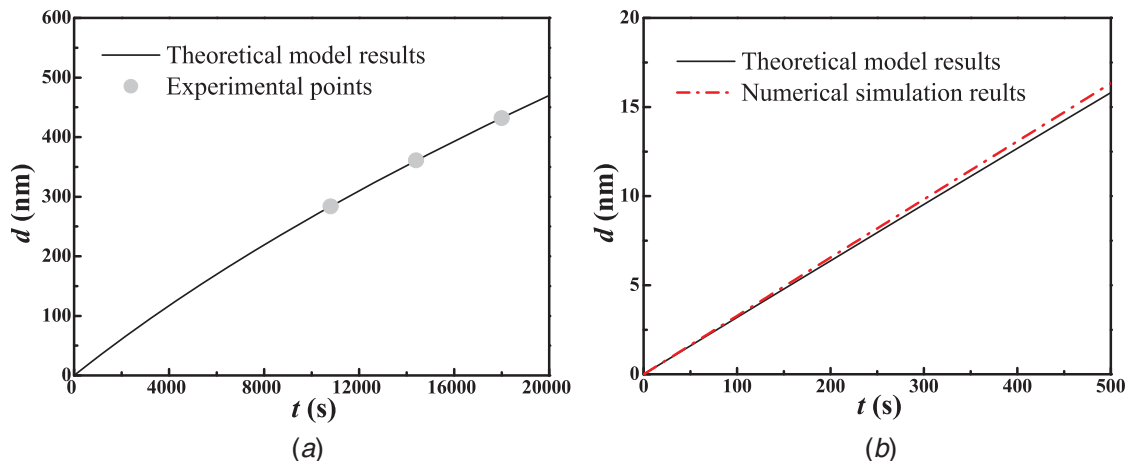

Fig. 4 Comparison of the growth of thickness over time: (a) theoretical and experimental results and (b) theoretical and numerical results
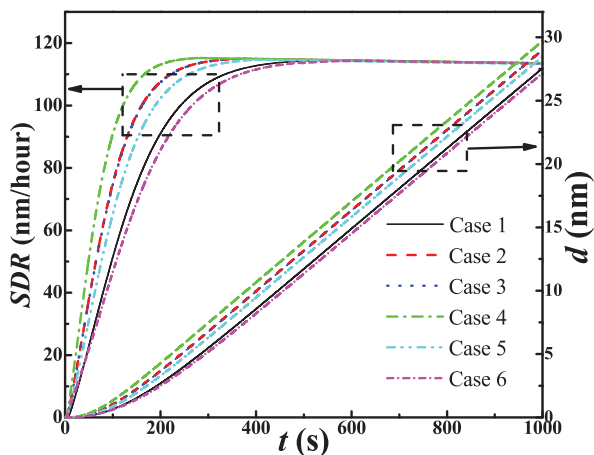
Fig. 5 Averaged surface deposition rate and thickness of MAPbI₃ layer on the substrate over time for cases 1–6

becomes more stable with a mild drop. That is because at the beginning of the simulation, the reaction plenum is filled with N_2, and MAI vapor is introduced through the inlets. With time, more MAI molecules reach the substrates and react with the PbI_2 on the surface. The molecular concentration of MAI on the substrate surface increases with time, leading to the increasing surface deposition rate. After the N_2 becomes purged from the plenum, the rate of MAI concentration on the surface decreases and finally becomes stable. This is the point when the concentration of MAI for surface deposition becomes stable. However, with the continuing of the reaction, the thickness of the perovskite layer increases and the surface deposition rate decreases since the MAI molecules must diffuse through the perovskite layer to react with the PbI_2. Therefore, the surface deposition rate drops regularly with time after all the N_2 is purged. Comparing cases 1–4, we can see that the surface deposition of case 4 increases most rapidly, and case 1 increases most slowly. Cases 2 and 3 have almost the same surface deposition rate. Therefore, the thickness of case 4 is larger than those of cases 1–3 during the period simulated (1000 s). This leads to a lower surface deposition rate of case 1 after the molecular concentration of MAI becomes stable in the plenum, which is hard to see in Fig. 6 as the thickness differences are small. The turning point of the SDR curve for case 4 appears earlier than for cases 2 and 3, and the turning points of the SDR curves for cases 2 and 3 appear earlier than for case 1, which means that case 1 can purge the N_2 from the plenum more quickly than cases 2 and 3 can, and cases 2 and 3 can purge the

N_2 from the plenum quicker than case 1 can. Comparing cases 4–6, we can see that the surface deposition of case 4 increases the fastest, and case 6 increases the slowest. This is because case 4 has three MAI inlets, while case 5 has two MAI inlets and case 6 has one MAI inlet. Case 4 has higher mass flowrate of MAI than cases 5 and 6, and therefore, case 4 has a higher surface deposition rate at the times before the N_2 is purged. Also, we can see that the turning point of the SDR curve for case 5 appears earlier than that for case 1, which means that adding screens can help purge the N_2 and the consumption of MAI is reduced.

Figure 6 shows the surface deposition rate distributions on the left substrate for cases 1–6 at 80 s and 320 s. When $t = 80$ s, a comparison of cases 1–4, we can see that case 4 has the highest surface deposition rate, while case 1 has the lowest. Cases 2 and 3 have similar surface deposition rates. This shows that adding screens helps in purging the N_2 more quickly and brings more MAI to the substrate. Comparing cases 4–6, we can see that case 4 has the highest surface deposition rate and case 6 has the lowest. For case 5, the surface deposition rate on the left is higher than that on the right, while for case 6, the surface deposition rate on the right is higher than that on the left. This is because case 5 has inlets 1 and 3 open, and case 6 has only inlet 2 open. The left side of the substrate of case 5 is closer to the MAI inlet, while the right side of the substrate of case 6 is closer to the MAI inlet. This means that the MAI vapor flow is highly influenced by the geometry. When $t = 320$ s, most of the N_2 has already been purged, and the differences in the surface deposition rate between different cases become smaller. All the cases, including cases 5 and 6, show a uniform distribution of the surface deposition rate on the substrate.

To analyze the uniformity of the surface deposition rate on the substrate, we define a new parameter called surface deposition rate deviation to show the deviation of the local surface deposition rate (SDR) from the averaged value ($\overline{SDR}$), as follows:

$$SDRD = \frac{SDR - \overline{SDR}}{\overline{SDR}} \qquad (18)$$

Figure 7 shows the surface deposition rate deviations on the left substrate for cases 1–6 at 80 s and 320 s. When $t = 80$ s, comparing cases 1–4, we can see that case 4 has the most uniform surface deposition rate distribution. Cases 2 and 3 have similar uniformity. Case 1 is the least uniform. Comparing cases 4–6, we can see that cases 5 and 6 have poor uniformity of the surface deposition rate, because the molecular concentration of MAI is higher near the mass flow inlets. When $t = 320$ s, the surface deposition rate deviation becomes very small for all the cases, as most of N_2 has been purged out.
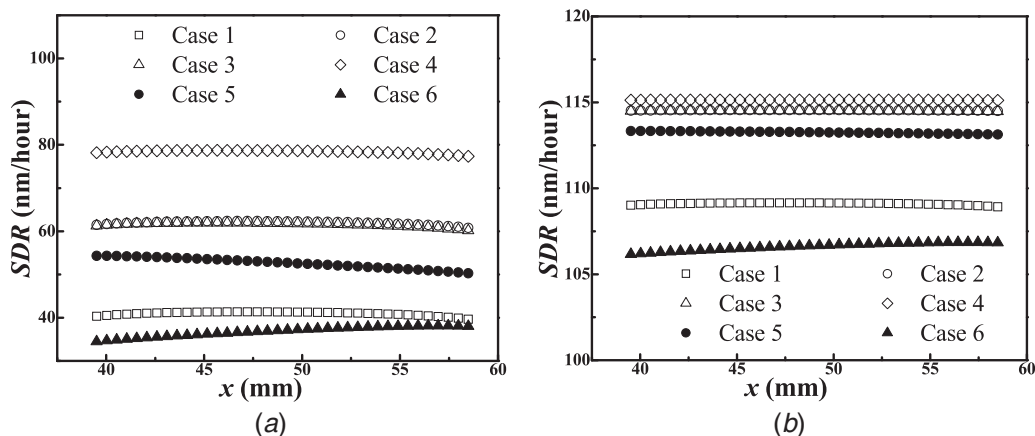

Fig. 6 Surface deposition rate distributions on the left substrate for cases 1–6 at (a) $t = 80$ s and (b) $t = 320$ s
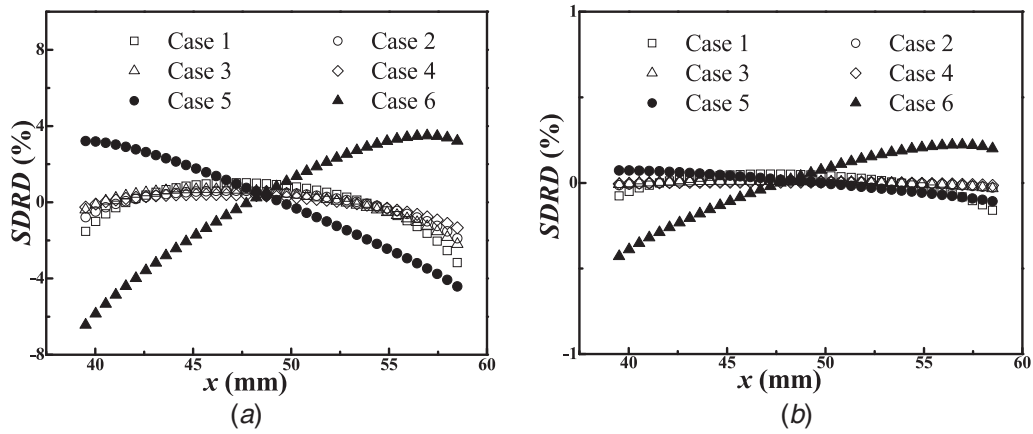
Fig. 7 Surface deposition rate deviations on the left substrate for cases 1–6 at (*a*) *t* = 80 s and (*b*) *t* = 320 s

Figure 8 shows contours of pressure and streamlines for cases 1–6 at *t* = 80 s. From cases 1–4, we can see the influence of adding screens. For case 2, there is a pressure drop on the upper screen (screen 1), and the streamlines of MAI are forced to distribute more uniformly across the screen, especially for the MAI from the middle inlet (inlet 2). The distribution of the streamlines below the screen is also influenced. For case 3, the pressure drop occurs on the lower screen (screen 2), and the distribution of streamlines is more uniform above the screen, compared with case 1, especially for the MAI from the inlets on the left and right (inlets 1 and 3).
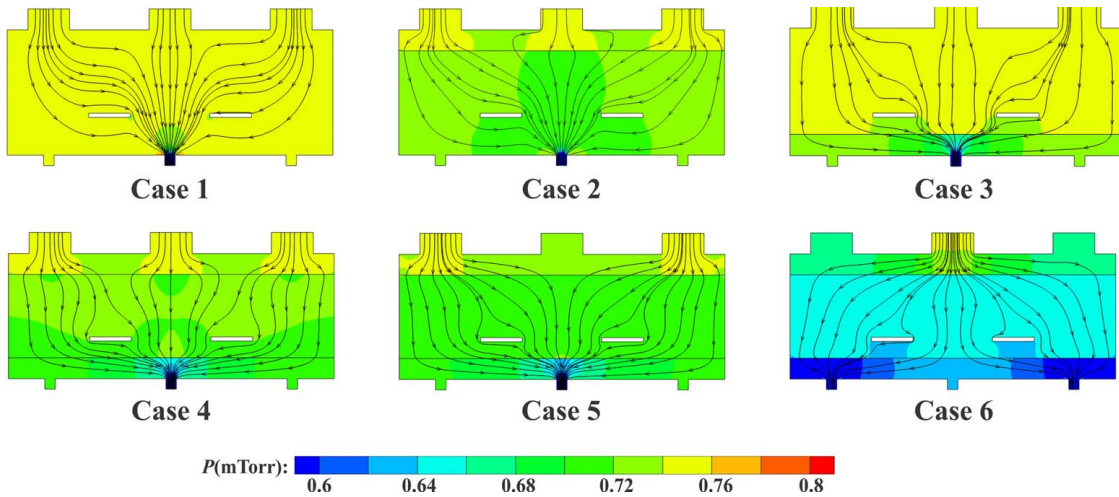

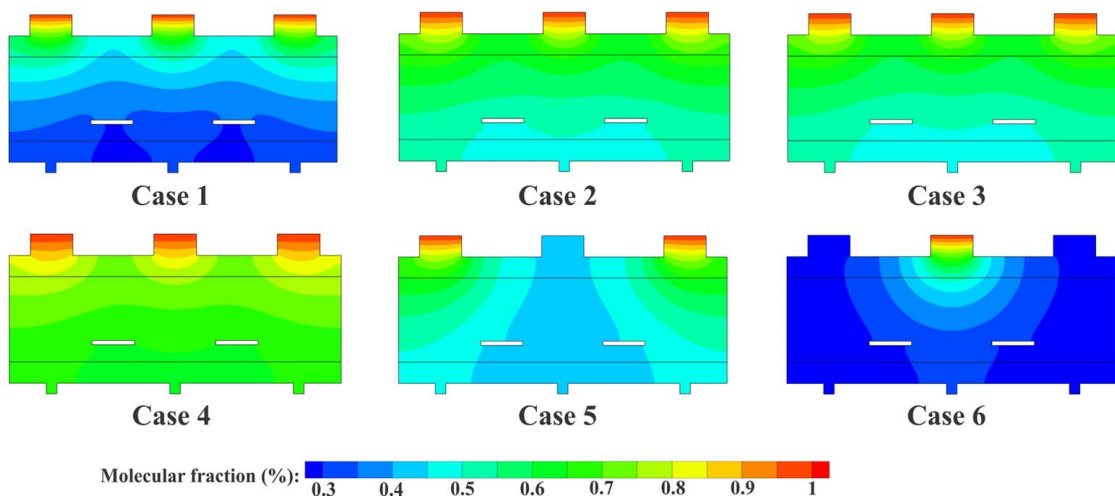**Fig. 8 Contours of pressure and streamlines for cases 1–6 at *t* = 80 s**

Fig. 9 Contours of molecular fraction of MAI for cases 1–6 at *t* = 80 s

After adding both screens, like case 4, we can see that the streamlines between the two screens are more uniform than in cases 1–3, which will make the MAI concentration distribution on the substrate more uniform. This explains why case 4 has a more uniform surface deposition rate than other cases. As for cases 5 and 6, the distribution of MAI concentration on the substrates is not as uniform as in cases 1–4, but we can see that most of the streamlines will pass the substrates, while for cases 1–4, most of the MAI from the middle inlet flows directly out through the middle outlet. This explains why cases 5 and 6 have more than 2/3 and 1/3 of the surface deposition rate, respectively, with only 2/3 and 1/3 of the mass flowrate of case 4.

Figure 9 shows contours of mole fraction of MAI for cases 1–6 at $t = 80$ s. Comparing cases 1–4, we can see that case 4 has the highest mole fraction of MAI, while case 1 has the lowest, and cases 2 and 3 have similar mole fraction values. This explains why case 4 has a higher surface deposition rate than the other cases at the same time. This is due to the screens that make the MAI vapor flow more uniform in the plenum, and then, the N_2 near the wall and in the corner can be mixed with MAI vapor and purged out more efficiently than in case 1 (without screens). Case 5 has a lower mole fraction of MAI in the middle part, while case 6 has a higher mole fraction of MAI in the middle part. Therefore, on the left substrate, the surface deposition rate of case 5 increases from left to right, while the surface deposition rate of case 6 decreases from left to right, as shown in Fig. 6(a).

4 Conclusions

A numerical model is established to simulate the vapor deposition process in the fabrication of a perovskite solar cell. The diffusion process of MAI vapor through the growing perovskite layer is part of the analysis. It employs a diffusion coefficient calculated from measurements of the growth of a perovskite layer in a deposition cell that is the same as the one analyzed. To the authors' knowledge, this is the first evaluation of diffusivity of MAI through the perovskite used herein. The simulation of the vapor deposition chamber is used to improve the deposition process. One feature is the use of screens. Their influence when positioned at various locations in the plenum is analyzed. The influences of inlets and outlets, numbers, and locations, are also quantified. The following conclusions are presented:

(1) In the vapor deposition process of a perovskite solar cell, the overall surface deposition rate will first increase, as the MAI concentration increases in the plenum. After N_2 is purged, the MAI concentration becomes stable within the plenum, but the surface deposition rate will decline with time because of the increasing thickness of the perovskite layer making the diffusion process slow.

(2) Adding screens makes the MAI vapor flow more uniform in the plenum and quickens the purge rate of N_2 precursor gas, leading to higher and more uniform surface deposition rate in the early part of the vapor deposition process.

(3) The flow of MAI vapor has a very low Reynolds number, and the flow is highly influenced by the geometry. Therefore, the effects of geometry of the reaction plenum, including the number and locations of MAI inlets, substrates, and outlets should be well understood toward achieving a design that gives a uniform and controlled surface deposition rate of the perovskite layer.

Acknowledgment

Data Availability Statement

The datasets generated and supporting the findings of this article are obtainable from the corresponding author upon reasonable request. The authors attest that all data for this study are included in the paper. Data provided by a third party listed in Acknowledgments. No data, models, or code were generated or used for this paper.

References

[1] Akihiro, K., Kenjiro, T., Yasuo, S., and Tsutomu, M., 2009, "Organometal Halide Perovskites as Visible-Light Sensitizers for Photovoltaic Cells," J. Am. Chem. Soc., **131**(17), pp. 6050–6051.

[2] The National Renewable Energy Laboratory (NREL), 2019, https://www.nrel.gov/pv/assets/pdfs/best-research-cell-efficiencies.20190802.pdf

[3] Wojciechowski, K., Saliba, M., Leijtens, T., Abate, A., and Snaith, H. J., 2014, "Sub-150 °C Processed Meso-Superstructured Perovskite Solar Cells With Enhanced Efficiency," Energy Environ. Sci., **7**(3), pp. 1142–1147.

[4] Ray, R., Sarker, A. S., and Pal, S. K., 2019, "Improving Performance and Moisture Stability of Perovskite Solar Cells Through Interface Engineering With Polymer-2D MoS$_2$ Nanohybrid," Sol. Energy, **193**, pp. 95–101.

[5] Wang, J. T., Ball, J. M., Barea, E. M., Abate, A., Alexander-Webber, J. A., Huang, J., Saliba, M., Mora-Sero, I., Bisquert, J., Snaith, H. J., and Nicholas, R. J., 2013, "Low-Temperature Processed Electron Collection Layers of Graphene/TiO$_2$ Nanocomposites in Thin Film Perovskite Solar Cells," Nano Lett., **14**(2), pp. 724–730.

[6] Duan, J., Wu, J., Zhang, J., Xu, Y., and Lund, P. D., 2016, "TiO$_2$/ZnO/TiO$_2$ Sandwich Multilayer Films as a Hole-Blocking Layer for Efficient Perovskite Solar Cells," Int. J. Energy Res., **40**(6), pp. 806–813.

[7] Yang, L., Yang, P., Wang, J., Hao, Y., Li, Y., Lin, H., and Zhao, X., 2019, "Low-Temperature Preparation of Crystallized Graphite Nanofibers for High Performance Perovskite Solar Cells," Sol. Energy, **193**, pp. 205–211.

[8] Ying, C., Shi, C., Wu, N., Zhang, J., and Wang, M., 2015, "A Two-Layer Structured pbi2 Thin Film for Efficient Planar Perovskite Solar Cells," Nanoscale, **7**(28), pp. 12092–12095.

[9] Li, Y. B., Cooper, J. K., Buonsanti, R., Giannini, C., Liu, Y., Toma, F. M., and Sharp, I. D., 2015, "Fabrication of Planar Heterojunction Perovskite Solar Cells by Controlled Low-Pressure Vapor Annealing," J. Phys. Chem. Lett., **6**(3), pp. 493–499.

[10] Subbiah, A. S., Halder, A., Ghosh, S., Mahuli, N., Hodes, G., and Sarkar, S. K., 2014, "Inorganic Hole Conducting Layers for Perovskite-Based Solar Cells," J. Phys. Chem. Lett., **5**(10), pp. 1748–1753.

[11] Kim, B. S., Kim, T. M., Choi, M. S., Shim, H. S., and Kim, J. J., 2015, "Fully Vacuum–Processed Perovskite Solar Cells With High Open Circuit Voltage Using MoO$_3$/NPB as Hole Extraction Layers," Org. Electron., **17**, pp. 102–106.

[12] Zhao, D., Ke, W., Grice, C. R., Cimaroli, A. J., Tan, X., Yang, M., Collins, R. W., Zhang, H., Zhu, K., and Yan, Y., 2015, "Annealing-Free Efficient Vacuum-Deposited Planar Perovskite Solar Cells With Evaporated Fullerenes as Electron-Selective Layers," Nano Energy, **19**, pp. 88–97.

[13] Chen, Q., Zhou, H., Hong, Z., Luo, S., Duan, H. S., Wang, H. H., Liu, Y., Li, G., and Yang, Y., 2014, "Planar Heterojunction Perovskite Solar Cells via Vapor-Assisted Solution Process," J. Am. Chem. Soc., **136**(2), pp. 622–625.

[14] Chen, Q., Zhou, H., Song, T. B., Luo, S., Hong, Z., Duan, H. S., Dou, L., Liu, Y., and Yang, Y., 2014, "Controllable Self-Induced Passivation of Hybrid Lead Iodide Perovskites Toward High Performance Solar Cells," Nano Lett., **14**(7), pp. 4158–4163.

[15] Zhou, H., Chen, Q., and Yang, Y., 2015, "Vapor-Assisted Solution Process for Perovskite Materials and Solar Cells," MRS Bull., **40**(8), pp. 667–673.

[16] Wang, S., Ono, L. K., Leyden, M. R., Kato, Y., Raga, S. R., Lee, M. V., and Qi, Y. B., 2015, "Smooth Perovskite Thin Films and Efficient Perovskite Solar Cells Prepared by the Hybrid Deposition Method," J. Mater. Chem. A, **3**(28), pp. 14631–14641.

[17] Leyden, M. R., Ono, L. K., Raga, S. R., Kato, Y., Wang, S., and Qi, Y., 2014, "High Performance Perovskite Solar Cells by Hybrid Chemical Vapor Deposition," J. Mater. Chem. A, **2**(44), pp. 18742–18745.

[18] Leyden, M. R., Lee, M. V., Raga, S. R., and Qi, Y. B., 2015, "Large Formamidinium Lead Trihalide Perovskite Solar Cells Using Chemical Vapor Deposition With High Reproducibility and Tunable Chlorine Concentrations," J. Mater. Chem. A, **3**(31), pp. 16097–16103.

[19] Peng, Y., Jing, G., and Cui, T., 2015, "A Hybrid Physical-Chemical Deposition Process at Ultra-Low Temperatures for High-Performance Perovskite," J. Mater. Chem. A, **3**(23), pp. 12436–12442.

[20] Wehrenfennig, C., Liu, M., Snaith, H. J., Johnston, M. B., and Herz, L. M., 2014, "Charge-Carrier Dynamics in Vapour-Deposited Films of the Organolead Halide Perovskite CH$_3$NH$_3$PbI$_{3-X}$Cl$_X$," Energy Environ. Sci., **7**(7), pp. 2269–2275.

[21] Jeon, N. J., Noh, J. H., Kim, Y. C., Yang, W. S., Ryu, S., and Seok, S. I., 2014, "Solvent Engineering for High-Performance Inorganic–Organic Hybrid Perovskite Solar Cells," Nat. Mater., **13**(9), pp. 897–903.

[22] Agrafiotis, C., Pein, M., Giasafaki, D., Tescari, S., Roeb, M., and Sattler, C., 2019, "Redox Oxides-Based Solar Thermochemistry and Its Materialization to Reactor/Heat Exchanger Concepts for Efficient Solar Energy Harvesting, Transformation and Storage," ASME J. Sol. Energy Eng., **141**(2), p. 021010.

[23] Udayabhaskararao, T., Kazes, M., Houben, L., Lin, H., and Oron, D., 2017, "Nucleation, Growth, and Structural Transformations of Perovskite Nanocrystals," Chem. Mater., **29**(3), pp. 1302–1308.

[24] Xue, H., Bergirsson, E., and Stangl, R., 2019, "Correlating Variability of Modeling Parameters With Photovoltaic Performance: Monte Carlo Simulation of a Meso-Structured Perovskite Solar Cell," Appl. Energy, **237**, pp. 131–144.

[25] Yang, C., Simon, T., and Cui, T., 2017, "Numerical Simulation and Analysis of Hybrid Physical-Chemical Vapor Deposition to Grow Uniform Perovskite MAPbI$_3$," J. Appl. Phys., **121**(14), pp. 1989–1997.

[26] Arivazhagan, V., Xie, J., Yang, Z., Hanga, P., Parvathia, M. M., Xiao, K., Cui, C., Yang, D., and Yu, X., 2019, "Vacuum Co-Deposited CH$_3$NH$_3$PbI$_3$ Films by Controlling Vapor Pressure for Efficient Planar Perovskite Solar Cells," Sol. Energy, **181**, pp. 339–344.

[27] Joback, K. G., and Reid, R. C., 1987, "Estimation of Pure-Component Properties From Group-Contributions," Chem. Eng. Commun., **57**(1), pp. 233–243.

[28] Curtiss, C. F., Hirschfelder, J. O., and Bird, R. B., 1954, *Molecular Theory of Gases and Liquids*, John Wiley & Sons, New York.

[29] Onoda-Yamamuro, N., Matsuo, T., and Suga, H., 1992, "Dielectric Study of CH$_3$NH$_3$Pbx$_3$ (x = Cl, Br, I)," J. Phys. Chem. Solids, **53**(7), pp. 935–939.

[30] Idel'chik, I. E., and Steinberg, M. O., 1996, *Handbook of Hydraulic Resistance*, 4th ed., Begell House, New York.

[31] Wang, B., Young Wong, K., Xiao, X., and Chen, T., 2015, "Elucidating the Reaction Pathways in the Synthesis of Organolead Trihalide Perovskite for High-Performance Solar Cells," Sci. Rep., **5**(1), p. 10557.

[32] Wei, X., Peng, Y., Jing, G., and Cui, T., 2018, "Planar Structured Perovskite Solar Cells by Hybrid Physical Chemical Vapor Deposition With Optimized Perovskite Film Thickness," Jpn. J. Appl. Phys., **57**(5), p. 052301.